

ACCEPTED MANUSCRIPT

Final published version of this article:

[Journal of Materials Science: Materials in Electronics](#) Volume 32, pages 1818–1828, (2021)

Available online: 02 january 2021

DOI: <https://doi.org/10.1007/s10854-020-04950-y>

Defect states in ZnO/SnO₂ composite nanostructures (CNs) for possible facilitating role in carrier transport across the junction

[Madiha Sabeen](#)¹, [Liaquat Aziz](#)¹, [Tahir Nazir](#)¹, [Shahid Mehmood](#)¹, [Muhammad Fahad Bhopal](#)¹, [Awais Ali](#)¹, [Faisal Saeed](#)¹, [Faisal Nasim](#)¹, [C. Cepek](#)², [S. Bhardwaj](#)², [Anwar Ul-Hamid](#)³ & [Arshad Saleem Bhatti](#)¹

1-Department of Physics, Centre for Micro and Nano Devices (CMND), COMSATS University Islamabad, Park Road, Islamabad 44000, Pakistan

2- CNR-IOM, Laboratorio TASC, StradaStatale 14, Km 163.5, 34149 Trieste, Italy

3- Center for Engineering Research, Research Institute, King Fahd University of Petroleum & Minerals, Dhahran 31261, Saudi Arabia

ABSTRACT

This paper explores the possible role of defect states in charge transport in a type II heterointerface formed by ZnO/SnO₂ composite nanostructures (CNs) grown using VLS technique. XRD and high-resolution TEM analysis revealed the granular growth of SnO₂ in a matrix of ZnO. Raman spectra obtained from CNs were marked by the presence of oxygen vacancies as Raman modes were broadened and shifted. XPS results confirmed the presence of oxygen vacancies in ZnO and SnO₂ and Zn interstitials in ZnO, which showed dependence on growth temperature. Photoluminescence (PL) spectra acquired from CNs were marked by the presence of a very broad PL band in the visible region centered around 2.4 eV, while a very weak near-band-edge emission was observed. The PL band in the visible region showed contributions from Zn interstitials (2.4–2.6 eV) and oxygen vacancies (1.9–2.1 eV) in ZnO, and the PL band of SnO₂ consisted of primarily oxygen vacancies (1.9–2.1 eV). The PL bands obtained from CNs showed the absence of Sn interstitials in SnO₂. The photoluminescence excitation (PLE) spectrum taken from CNs clearly showed absorption in the band gap due to defects. The role of defect states in the charge transfer process in type II heterostructures was further studied by electrical measurements on SnO₂/ZnO bilayer thin films. Temperature-dependent I–V characterization showed significant accumulation of charges at the interface, which was released by thermal excitation. It is, therefore, concluded that defects can play a positive role in photocatalytic devices, where excess charge is needed at the interface for catalytic reaction.

1 Introduction

Wide band-gap semiconductor composite nanostructures (CNs) with type-II band alignment such as ZnO/TiO₂, SnO₂/Fe₂O₃, TiO₂/SnO₂, to name a few, consist of two semiconductors with staggered band alignments. Such heterojunctions are widely studied for effective charge transfer across the heterojunction for processes that require charge separation, such as photocatalysis, solar energy harvesting, etc. In type II band alignment, electrons (holes) are transferred from one semiconductor with higher conduction (lower valence) band to that with lower conduction (higher valence) band. The interface of the heterostructures forms the active region, which facilitates in the charge transport process. The rate of the charge transport process depends on the quality of the interface as it can promote or hinder the transfer rates. In oxide semiconductor heterostructures like ZnO/SnO₂, the situation becomes complex due to intrinsic defects created by vacancies and interstitials such as

oxygen vacancies (V_o), interstitials (zinc interstitial (I_{Zn}), tin interstitials (I_{Sn})), and oxygen antisites (O_{Zn} , and O_{Sn}). The defect states of V_o , I_{Zn} , and I_{Sn} , which form energy states below the CB edge make an effective place for storage of charges and thus control the efficiency of transfer of carriers across the heterointerface [1]. It has been reported that most of these defects are optically active and are responsible for visible emission from these wide band-gap oxide semiconductors. These defects also provide a channel for carriers to recombine with photoexcited holes in the valence band [2, 3].

One-dimensional (1-D) nanomaterials such as nanorods, nanowires, nanofibers, and nanotubes have gained enormous interest because of their unique and usual properties as well as their potential applications in functional devices [4]. Among 1-D nanostructured oxide semiconductors, zinc oxide (ZnO) and tin oxide (SnO_2) are wide-energy bandgap semiconductors, with a reported energy gap of 3.37 [5] and 3.6 eV [6], respectively. Both of these oxide semiconductors behave intrinsically like n-type semiconductors, which are attributed to the presence of oxygen vacancies (V_o) and interstitial (I_{Zn}) and (I_{Sn}) sites. ZnO and SnO_2 follow similar crystal growth kinematics, and thus ZnO/ SnO_2 composite nanostructures (CNs) can easily be synthesized. Many investigators employed various synthesis methods to obtain ZnO/ SnO_2 CNs including vapor liquid solid technique (VLS) [7], hydrothermal method [8], and sol-gel technique [9].

In recent years, oxide semiconductors as standalone or their composites with other semiconductors or metals (like Au) have shown enhanced photocatalytic properties. For example, NiO and Co_3O_4 [10], CuO [11], and TiO_2 [12] NSs were used for high photocatalytic activity. Similar, Au coated TiO_2 has also been used for efficient photocatalysis as a result of exciton plasmon coupling [13]. A number of reports have demonstrated that ZnO/ SnO_2 CNs show improved properties such as conversion efficiency in solar cells, enhance photocatalytic activity, and improved gas sensing due to enhanced charge transport properties. This was mainly attributed to the type II band alignment in ZnO/ SnO_2 [14] and mechanism of charge transfer, which was explained using the Z-scheme charge transfer mechanism, where electrons flow from the semiconductor with low conduction band edge and high Fermi energy to the semiconductor with high conduction band edge with low Fermi energy [15] to form a depletion region. In the absence of defects, these carriers recombine with holes of second semiconductor instantaneously; however, the situation changes drastically in the presence of defects at the interface. The trap states at the interface of ZnO/ SnO_2 impede the charge transport process and slow the transfer rates. The trap centers also act as scattering centers to further reduce the mobility in type II heterostructures [16].

The presence of defects at the interface strongly affects process of charge transfer across the junction and may lead to either charge accumulation at the interface or recombination through the defects assisted luminescence. This leads to degradation of electrical characteristics of the heterojunction devices. Many factors affect the charge transport across the ZnO/ SnO_2 heterointerface, i.e., Columbic scattering and interface traps. [17]. Thus, the knowledge of density and behavior of defects at the interface become quite crucial in the performance of devices working at different temperatures [18].

This paper reports the synthesis of ZnO/ SnO_2 CNs employing vapor-liquid-solid (VLS) technique at four different growth temperatures with Sn being used as catalytic seed. Structural and morphological characterizations were done with X-ray diffraction technique and transmission electron microscopy, respectively. Raman spectroscopy was used to study the vibrational modes of ZnO and SnO_2 in CNs. X-ray photoelectron spectroscopy (XPS) was used to determine the oxidation states and chemical composition of ZnO and SnO_2 in CNs. The optical properties of defects in CNs were studied by performing photoluminescence and photoluminescence excitation spectroscopy. An

insight into the charge transport process across the interface was gained by performing temperature-dependent $I-V$ measurements on ZnO/SnO₂ planar films.

2 Experiment

Four Si (101) substrates were cleaned with RCA procedure, and 3 nm Sn was deposited in a high vacuum chamber at the working pressure of 10^{-5} tors. The source material composed of ZnO:graphite (1:0.25) (SnO₂:graphite (1.0.25)) powders was loaded in an alumina boat and placed in the center of the horizontal tube furnace. The Sn (3 nm)-coated Si substrates were placed in the tube furnace at some distances from the center where temperatures were * 970 C (S1), 990 C (S2), 1010 C (S3), and 1020 C (S4), respectively, after which temperature of the furnace was raised to 1150 C in the presence of a flowing nitrogen gas at a constant flow rate of 25 Sccm. The dwell time for the synthesis process was two hours after which the furnace was allowed to cool down in flowing gas. ZnO/SnO₂ heterojunction thin films were prepared on indium tin oxide (ITO) coated glass substrate by dip-casting method. One molar solution of ZnO was prepared in methanol while of SnO₂ was prepared in toluene and sonicated for half hour. Then thin-film heterojunction was annealed at 300 C. Two Al contacts were made, one on the bottom of ZnO on ITO surface and second on top of SnO₂ film.

Fluorescence images were taken by Olympus BX3 optical microscope attached with DP 25 camera using TX-red filter. The crystal phase analysis was carried out by PANalytical's X'Pert Pro X-ray diffractometer with Cu-K α source ($k = 1.5406 \text{ \AA}$). The high-resolution transmission electron microscopy was performed by JEOL (model JEM 2100F) operating at 200 keV. The Raman and PL spectra were collected from LABRAM III (Dongwoo Optron) using aircooled Ar²⁺ ion laser with an excitation wavelength of

514 nm and He-Cd laser with an excitation wavelength of 325 nm, respectively. PLE spectroscopy (Dangwoo Optron macro PLE, EL system SEL001) was carried out using Xe lamp running at 400 W. The XPS spectra were recorded in a homemade system equipped in an ultra-high vacuum chamber at room temperature in normal emission geometry using a Mg-K α X-ray source ($h\nu = 1253.6 \text{ eV}$) with a 120 mm hemispherical electron energy analyzer and overall energy resolution of * 0.8 eV. $I-V-T$ measurements on thin-film ZnO/SnO₂ heterojunction were performed with MDC's $C-V$ system equipped with Keithley's 237 source meter. Each scan was swept from - 30 V to ? 30 V with a step size of 0.3 V in a temperature range from 40 to 200 C, and Au-plated chuck and tungsten microprobes were used to make top and bottom contacts, respectively.

3 Results and discussion

3.1 Optical microscopy

The fluorescence images of ZnO/SnO₂ CNs synthesized at four temperatures (Fig. 1), S1 * 970 C, S2 * 990 C, S3 * 1010 C, and S4 * 1020 C showed blue-green, orange, and red emissions with varied intensities. The emission in the visible region was ascribed to various intrinsic defects as zinc interstitials (I_{Zn}), tin interstitials (I_{Sn}), oxygen vacancies (V_o), and oxygen antisites (O_{Zn} and O_{Sn}) in CNs.

3.2 X-ray diffraction

The XRD patterns obtained from the four ZnO/SnO₂ CNs are plotted in Fig. 2a, which showed major reflections from ZnO, SnO₂, and a minute impurity phase ZnSnO₃. The diffraction peaks located at 31.90, 34.40, 36.25, 47.60, and 56.66 were indexed as (100), (002), (101), (102), and (110) planes of hexagonal ZnO (JCPD: 01-080-0075), respectively. The peaks observed at 26.08, 32.49, and 55.47 were assigned to (110), (101), and (002) reflection planes of tetragonal SnO₂ (JCPD: 00-041-1445), respectively. The diffraction peaks observed at 28.07, 51.70, and 55.07 were identified as (220), (422), and (511) planes of hexagonal ZnSnO₃ (JCPD: 01-089-0095), respectively. ZnSnO₃ peaks were only observed in only two samples grown at 970 C and 990 C. As peaks corresponding to the ZnO were dominating, the ZnO-rich samples were revealed as compared to SnO₂. The shift in the peak positions was analyzed from the point of substitution of Zn²⁺ (0.74 Å) ions in SnO₂ lattice and Sn⁴⁺ (0.69 Å) ions in ZnO lattice. A slight shift in the diffraction peaks observed in CNs at various temperatures with respect to the JCPD data was attributed to the creation of vacancies rather than substitution of Sn. As the magnitude of shift of peaks (* 1–2%) was smaller than the shift expected due to substitution of Zn in SnO₂ lattice (* 7%), the magnitude of vacancies were estimated from the XPS results.

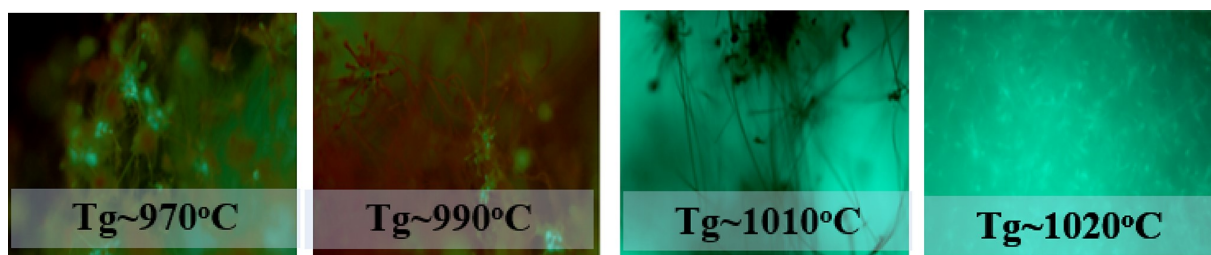


Fig. 1 Fluorescence images of ZnO/SnO₂ CNs synthesized at various temperatures

Williamson and Hall (WH) plots and Debye–Scherrer (DS) equation were used to determine the crystallite size and residual stress in the synthesized CNs and are plotted in Fig. 2b and c, respectively. W–H plots help to differentiate between size-induced and strain-induced peak broadening by considering the peak width as a function of 2θ [19], while Scherrer formula ($D = \frac{0.9}{\Delta k} \lambda$) uses the full width at half maximum of the major diffraction peak. Figure 2b shows that the crystallite size of ZnO and SnO₂ in CNs was determined by WH plots and DS equation. On average, the DS equation resulted in larger crystallite size, while WH plots showed smaller crystallite sizes of both ZnO and SnO₂ in composite NSs. However, the crystallite sizes of both ZnO and SnO₂ increased appreciably (five times in ZnO and three times in SnO₂) in composites grown at high temperatures. Variation in the crystallite size and strain was attributed to the internal modulation induced by V_o defects, which affected the extent of overlap between Zn-dangling bonds in the absence of oxygen atom [20]. This also resulted in the presence of Zn in the metallic form as observed in XPS spectra. The strain was also determined from the WH and DS equations and is plotted in Fig. 2c. The ZnO showed more or less very small change in the strain in NSs grown at different temperatures, while strain was much prominent and showed strong temperature dependence in SnO₂ NSs. This was attributed to strong variation in oxygen vacancies in SnO₂ NSs with growth temperatures as observed in the XPS results. The morphology of CNs was further studied by high-resolution transmission electron microscopy.

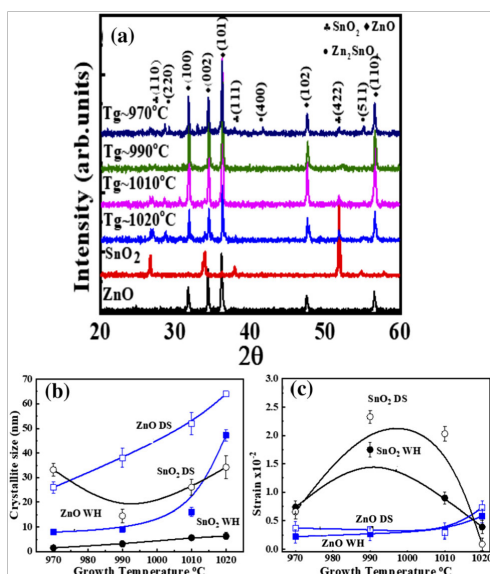


Fig. 2 a X-ray diffraction patterns of ZnO, SnO₂, and CNs grown at various temperatures. b crystallite sizes and c strain ZnO and SnO₂ in CNs determined from the Debye–Scherrer formula and W–H plots, respectively

3.3 High-resolution Transmission electron microscopy (HRTEM)

TEM was carried out to study the morphology, crystallinity, and interface between ZnO and SnO₂ in the synthesized CNs, and Fig. 3a shows the TEM image of CNs grown at 1020 C (S4), which mostly consist of belt-like structures. The average width of belts was around 30 ± 5 nm and length around 200 ± 10 nm. Figure 3b, c shows the high-resolution TEM images, and Fig. 3d shows the selected area electron diffraction (SAED) pattern taken from CNs grown at 1020 C. The HRTEM images clearly show two regions, bright and dark, which have been labeled as “Z” for ZnO and “S” for SnO₂. The interplanar distances of the two regions (as shown in the inset of Fig. 3b are used to identify the materials, and it was found that the white region was corresponded to ZnO, while the dark regions were corresponded to SnO₂.

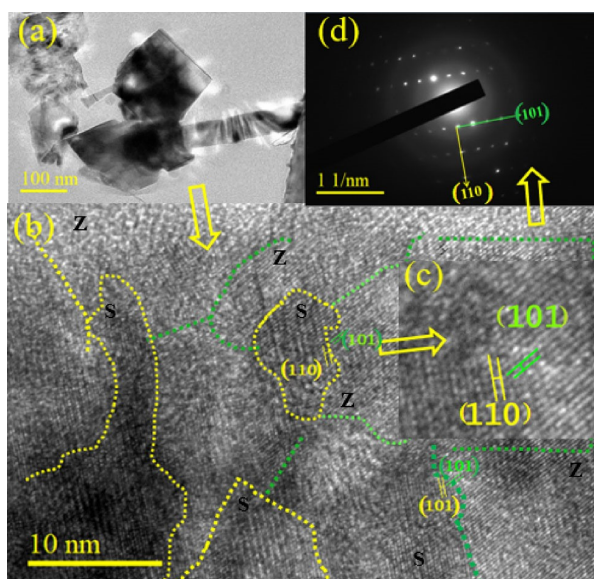


Fig. 3 a TEM image of CNs grown at 1020 °C, b HRTEM image of CNs, green boundary shows the ZnO regions, while yellow boundary shows SnO₂ regions, c enlarged area of part (b)

Figure 3c shows the amplified image where the “d” spacing was 0.24 nm, which corresponded to (101) plane of ZnO and 0.34 nm, which corresponded to (110) plane of SnO₂. The TEM images clearly showed the dominance of ZnO as host material, where SnO₂ was embedded in it. The boundaries between the two regions were clearly identified and were marked by dashed lines. Figure 3d shows the SAED pattern of the same sample, i.e., grown at 1020 °C, which showed that the synthesized CNs had wurtzite phase of ZnO with (101) preferred direction and tetragonal rutile phase of SnO₂ with (110) preferred direction. SAED patterns were also used to determine the interplanar spacing, which was 0.24 nm of the (101) planes of ZnO and 0.34 nm of the (110) planes of SnO₂. The HRTEM analysis of CNs grown at other temperatures confirmed the findings. For lack of space, the analysis is given in supplement information S1. Although TEM images showed clear boundaries between the two materials in the CNs; however, Raman spectroscopy was employed to see if there was any intermixing of two phases.

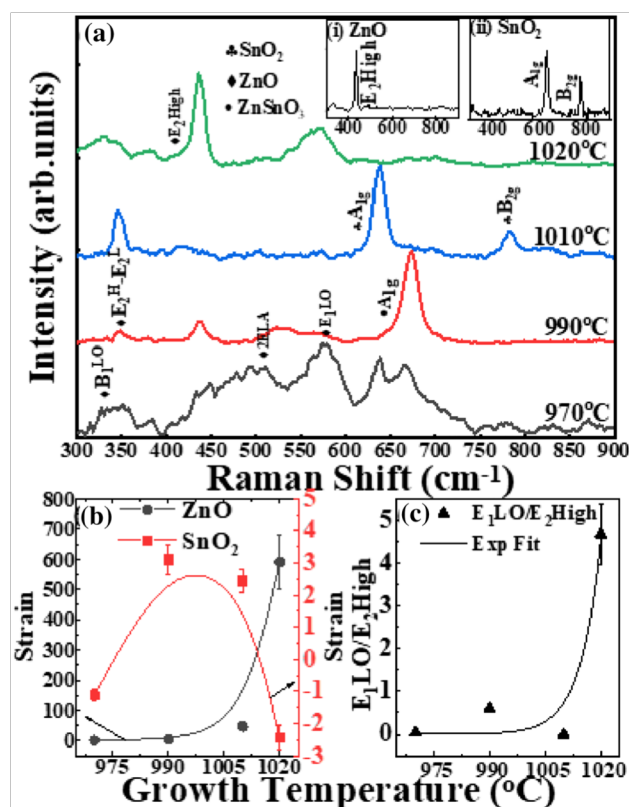


Fig. 4 a Raman spectra of CNs * grown at various temperatures. Insets (i) Raman spectra of ZnO; (ii) Raman spectra of SnO₂; b strain determined from the Leonard–Jones potential relation in d SAED pattern of CNs grown at 1020 °C CNs belongs to ZnO and SnO₂; c the ratio of E₁^{LO}/E₂^{High} modes of ZnO in CNs

3.4 Raman spectroscopy

Raman spectra of CNs grown at four temperatures are shown in Fig. 4a, where for reference, Raman spectra of ZnO and SnO₂ are also plotted. E₂^{High} and A_{1g} modes of hexagonal wurtzite ZnO and tetragonal rutile SnO₂ were observed, respectively. Raman spectra showed a slight red shift and broadening in the observed Raman modes in CNs grown at higher temperatures. The possible shift and width broadening were used in the Leonard–Jones potential relation to determine residual

strain. ZnSnO₃ modes were observed only at the lower growth temperature, i.e., 970 and 990 C. Figure 4(a) shows the peaks, at 333, 437, and 582 cm⁻¹ were assigned to E_{2δhighp}, E_{2δlowp}, E_{2δhighp}; and E_{1δLOp} Raman modes of ZnO, respectively [21]. The peaks observed at 630 and 779 cm⁻¹ were two fundamentals active Raman modes A_{1g} and B_{2g} of SnO₂, respectively [22]. Another band was observed at 670 cm⁻¹, was assigned to the A_{1g} mode of ZnSnO₃ [23], which was observed only in CNs grown at low temperatures, i.e., at 970 C and 990 C. The usual ZnO E_{2δhighp} E_{2δlowp} is related to lattice vibrations of zinc atoms [24]. The E_{2δhighp} mode was associated with the lattice vibration of oxygen atom attached with the Zinc atom in the tetrahedral coordinated. The strong E_{2δhighp} mode indicated high quality of crystallinity. The presence of E_{1δLOp} mode actually reflected the presence of oxygen deficiencies, i.e., V_o in ZnO [25]. The mode appeared at 571 cm⁻¹ is the ZnO longitudinal optical (LO) phonon mode having E₁ symmetry and shows the presence of V_o in ZnO in CNs, while E_{2δhighp} mode represents the vibration in lattice oxygen O–O bonds. Figure 4b shows the ratio of integrated intensities of the Raman modes E_{LO1} to that of E_{high2} (E_{LO1}=E_{high2}), which was more or less constant in CNs synthesized in the range 970 C to 1010 C and showed a sudden rise in the CNs grown at 1020 C as a result of increased V_o and decreased oxygen lattice (O_{lat}). In SnO₂, the A_{1g} and B_{2g} modes were related to the extension and compression oscillation of Sn–O bonds in the tetragonal rutile crystal structure.

Figure 4b shows the strain determined from the Raman modes of ZnO and SnO₂ in CNs using Leonard Jones potential relation $\propto \frac{1}{r} \left(\frac{a}{r} - 1 \right)^{-12} - \frac{b}{r} \left(\frac{a}{r} - 1 \right)^{-6}$, where “a” and “r” are the attractive and repulsive exponents in the potential of each bond. Here Zn–O bond length was taken as 1, the values of “a” and “r” were taken as 6 and 12 for the van der Waal’s bonds according to Leonard–Jones potential, 1 and 9 for ionic bonding and have a sum (a + r) of 3 for the covalent bonds. The bonding in ZnO and SnO₂ was considered to be covalent, and therefore, the relation between the new phonon frequency and the bulk frequency becomes $\propto \frac{1}{r} \left(\frac{a}{r} - 1 \right)^{-12} - \frac{b}{r} \left(\frac{a}{r} - 1 \right)^{-6}$ [26]. These results showed that there was a 0.5 ± 0.05 decrease in the strain for ZnO and 0.005 ± 0.001 decrease in strain for SnO₂ in CNs. The residual strains were produced because of substitution of Zn atoms in place of Sn atoms as both have more or less same atomic radii. XPS was employed to further confirm the elemental composition and concentration of defect states in CNs.

3.5 X-ray photoelectron spectroscopy (XPS)

XPS was performed to determine the chemical composition and existence of defects in ZnO/SnO₂ CNs. Figure 5a shows the XPS survey spectra of CNs grown at 970 C and 1020 C. The survey spectra showed all peaks corresponded to Sn, Zn, O, and C with no other impurities. C-1s peaks (not shown here) observed at 286.6 eV (285.7 eV) grown at 970 C (1020 C) were used to normalize (correction in energy scale) the energies. Figure 5b and c shows O-1s peaks from the two CNs, which were deconvoluted into four peaks. The peak position at the low binding energy was ascribed to oxygen lattice (O_{lat}) in ZnO/SnO₂ CNs. The component at the 530 eV binding energy corresponded to O_{lat} in Zn–O bond, while that at 531 eV corresponded to the O_{lat} in Sn–O bond. The peak at 532 eV corresponded to the V_o in ZnO, while that at 533 eV corresponded to V_o in SnO₂. The V_o in ZnO was associated with O²⁻ ions that were in oxygen-deficient regions within the ZnO [27]. Atomic concentration of O_{lat} in ZnO was 49% and that in SnO₂ was 18% in CNs grown at 970 C, while V_o in ZnO was 17% and V_o in SnO₂ was 12%. The atomic concentration of O_{lat} in ZnO was 53% and that in SnO₂ was 19% in CNs grown at 1020 C, and V_o in ZnO was 18% and V_o in SnO₂ was 9%. This finding revealed that the vacancies were sensitive to the growth temperature of CNs.

Figure 5d and e shows the high-resolution Zn2p peaks in ZnO obtained from CNs grown at 970 C and 1020 C. Zn-2p shows the doublet state of Zn-2p_{1/2} and Zn-2p_{3/2} at binding energies of 1044.15 eV and 1021.03 eV, respectively. Two Gaussian peaks were fitted in Zn-2p_{3/2}, which represented the

metallic Zn and oxidized Zn in CNs. In CNs grown at 970 °C, Zn metal state was 41% and ZnO states were 59%, which were 63% and 36%, respectively, There would be two possibilities for Zn metal: one was unreacted metal and other was interstitial Zn atoms (I_{Zn}) in CNs. Figure 5f and g shows two high-resolution peaks of Sn-3d_{5/2} and Sn-3d_{3/2} at binding energies of 486.5 eV and 495.5 eV in CNs grown at 970 C and 1020 C, respectively.

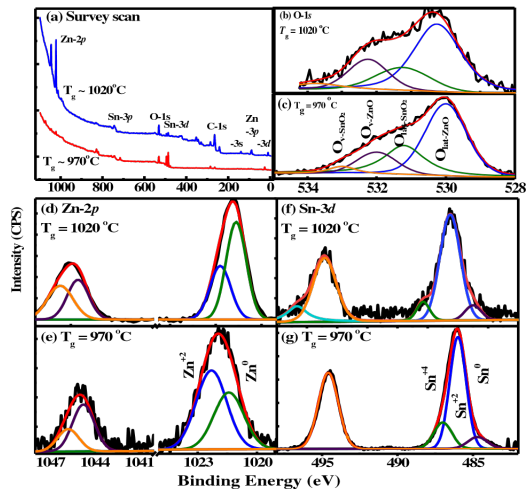


Fig. 5 a XPS survey spectrum, b, c O-1s, d, e Zn-2p, f, g Sn3d spectra fitted with Gaussian functions taken from CNs grown at 970 C and 1020 C.

Sn-3d_{5/2} peaks were further resolved into three peaks giving contributions of Sn metal state (484.55 eV), SnO₂ (487 eV) [28] and SnO (486.04), but the strength of SnO₂ state was much higher (70%) than the Sn metal state so Sn was fully oxidized in CNs grown at 970 C. However, in CNs grown at 1020 C, the Sn-3d peak showed that Sn was fully oxidized and formed SnO₂. It was observed that the two Sn-3d peaks were separated by 8.44 eV and showed that the chemical state was Sn⁴⁺ in SnO₂ [28]. It was observed that the binding energy difference in the two peaks decreased by 0.55 eV in ZnO and 0.08 eV in SnO₂ from the CNs grown at 970 °C to that was grown at 1020 °C. The binding energy difference was possibly due to variation in morphologies. The XPS results clearly demonstrated the formation of ZnO and SnO₂ along with existence of substantial amount of V_o, I_{Zn}, and I_{Sn} in CNs, which varied in concentration with the growth temperature. Photoluminescence excitation spectroscopy was used to determine the energy states created due to these intrinsic defects as discussed in the following section.

3.6 Photoluminescence excitation (PLE) spectroscopy

Figure 6 a–c shows the PLE spectra of the CNs grown at all temperatures and two reference samples ZnO and SnO₂, at different detection wavelengths (630, 750 nm). The selected detection wavelengths corresponded to different defect states. Figure 6a and b shows near-band-edge (NBE) emission of ZnO and SnO₂ observed at 3.29 eV and 3.90 eV, respectively, and absorption spectra (amplified) in the band gap at various energies are detected at 750 nm and 630 nm. The five dominant PLE peaks observed in ZnO belong to V_o in the range of 1.75 eV to 2.41 eV and I_{Zn} at 2.58 eV. Similarly, a weak absorption at 2.93 eV in SnO₂ was observed due to I_{Sn}. Figure 6c shows PLE spectra from the four CNs are detected at 630 nm and 750 nm. The near-band-edge absorption in ZnO at 3.29 eV and in SnO₂ at 3.87 eV was observed in all four CNs. The peaks in the PLE spectra marked by arrows in Fig. 6c

corresponded to ZnO spectra overall observed at 1.77 eV, 1.85 eV, 2.04 eV, and 2.41 eV due to V_o and at 2.58 eV due to I_{Zn} [29]. The absorption in the visible range was much stronger in ZnO than in SnO_2 due to higher defect density in ZnO as was determined from the XPS spectra. The SnO_2 absorption observed at 2.93 eV and 1.88 eV were broadened due to contributions from both ZnO and SnO_2 in CNs. The defect states determined from the PLE spectra of CNs, clearly showed that defect states in ZnO overwhelmed the defect states in SnO_2 .

states in SnO_2 .

3.7 Photoluminescence (PL) spectroscopy

Figure 7 shows the PL spectra obtained from pure ZnO, SnO_2 , and CNs. The PL spectrum from pure SnO_2 was quite different and broad compared to the PL spectrum from pure ZnO. However, the PL spectra obtained from CNs showed the same line shape as that of ZnO, except that in the UV region. Two distinct peaks/bands were observed in the PL spectra, one in the UV and second in the visible

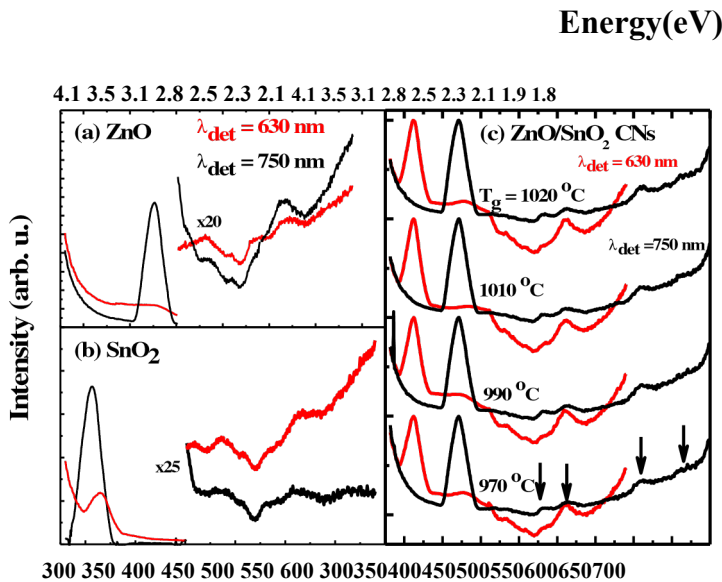


Fig. 6 Absorption peaks due to NBE and defect states of a ZnO, b SnO_2 , and c CNs detected at $\lambda_{det} = 630$ nm and 750 nm. The NBE absorption peaks in CNs that belong to SnO_2 and ZnO are observed at 325 nm and 370 nm, respectively. In (c) arrows mark the absorption due to defect states

region. The insets (i) and (ii) of Fig. 7 show the Gaussian fitting of the pure ZnO and SnO_2 PL spectra in the visible region. The PL spectrum from ZnO was resolved into four peaks with peak energies 2.6 eV, 2.4 eV, 2.1 eV, and 1.9 eV corresponding to defect states I_{Zn} , V_o , and V_o^b , respectively. The visible region of the PL spectrum from SnO_2 was also resolved into four peaks with peak energies 2.93 eV, 2.51 eV, 2.14 eV, and 1.95 eV corresponding to defect state I_{Sn} , V_o , and V_o^b , respectively [30]. The visible regions of CNs were deconvoluted into 3 peaks with energies 2.15 eV, 2.39 eV, and 2.58 eV corresponding to defect states I_{Zn} , V_o and V_o^b . The red emission band (1.95 eV) was related to deep-level defects within the gap of ZnO, associated with V_o^b while blue emission (2.93 eV) was related to the I_{Zn} and the green emission band represents the V_o in ZnO. The inset (iii) of Fig. 7 shows the plot of integrated intensities of the V_o contribution in four samples, where CNs grown at low temperature showed small amount of V_o and it increased in CNs grown at high temperatures. The PL results demonstrated the sensitivity of defect states on the growth

temperature. It was also observed that oxygen vacancies in ZnO overwhelmed oxygen vacancies in SnO₂ and that would affect the transfer of charge across the interface of two oxides.

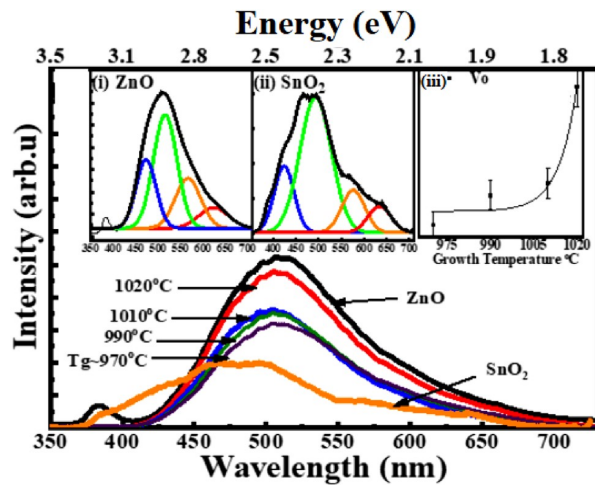


Fig. 7 PL spectra of ZnO, SnO₂ and CNs. Insets (i) Gaussian fitting of (i) ZnO PL spectrum; (ii) SnO₂ PL spectrum; and (iii) Integrated intensity of V_o in CNs grown at different temperatures. The fit shows the increase in V_o is exponential

3.8 I–V (T) measurements

In this section, the current-voltage (I–V) characteristics of ZnO-SnO₂ heterojunction thin films are presented and discussed in the temperature range of 40–200 C. It is well known that intrinsic SnO₂ is an n⁺ type as compare to intrinsic ZnO (n-type), so Schottky junction is formed between ZnO and SnO₂, when brought in thermal equilibrium. Electrons move from SnO₂ to ZnO and a built-in potential is established across the junction due to accumulation of charges. In the present case, as soon as an external circuit was made, current started flowing through the circuit, which was ascribed to the accumulated charges. The bias at which current was zero was considered as the built-in potential of the device.

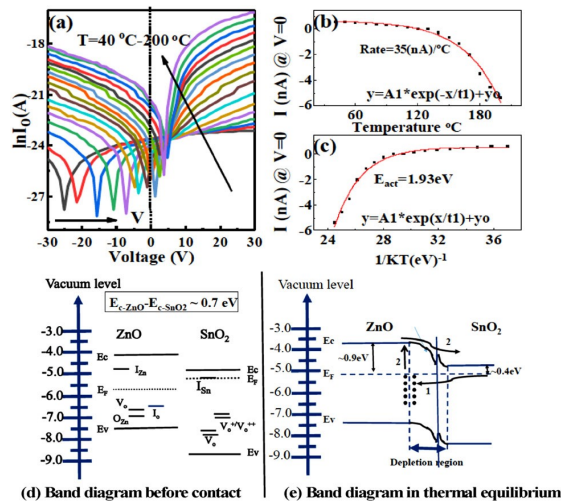


Fig. 8 a Plot of $\ln(I)$ at forward and reverse biases taken at various temperatures from 40 to 200 °C. b Plot of zero bias current as a function of device temperature. c Arrhenius plot of zero bias current for determination of activation energy. Band energy of ZnO/SnO₂ d before contact, and e in thermal equilibrium. The defect energy states are also given, which take part in photoluminescence and conduction. 1 and 2 represent the electron transfer routes on making contact and thermal escape, respectively

As the temperature was increased, the built-in potential started dropping and the current also started decreasing marginally as shown in Fig. 8b. As soon as the sign of the built-in potential changed to positive, the current also changed its sign and increased in the opposite direction rapidly as shown in Fig. 8b. The value of current (I) at zero bias (0 V) was plotted as a function of $(k_B T)^{-1}$ (Fig. 8c) to determine the activation energy of the carriers and it was 1.93 eV, which was more or less equal to the energy difference between the oxygen vacancies and conduction band minima of the ZnO. Figure 8d shows the band diagram of ZnO and SnO₂ before coming into contact. The diagram also shows the defect states and Fermi energy in two semiconductors, which is used to determine the charge transfer routes. A schematic of the current paths in thermal equilibrium and then at various temperatures is given in Fig. 8e. Path (1) represents the flow of charges from SnO₂ to ZnO on the formation of contact in thermal equilibrium. Path (2) represents the transfer of charges from the oxygen vacancies to the conduction band of ZnO and then to the conduction band of SnO₂. The sign of current changes when current following path (2) overcomes the current following route (1).

4 Conclusion

In this paper, we studied the intrinsic defects in ZnO/SnO₂ composite nanostructures for their possible role in the charge transport process across the type II heterojunction. XRD and Raman spectroscopy confirmed the mixed growth of ZnO (Hexagonal) and SnO₂ (tetragonal) in CNs. Heterointerface of ZnO and SnO₂ NS was clearly observed by HRTEM. XPS results indicated that Sn and Zn were in reduced states and thus showed existence of oxygen vacancies. The defect states in ZnO and SnO₂ were also observed in the PLE spectra of composites. PL spectra showed a broad band in the visible region, which was attributed to the defect states in CNs and was resolved to show blue, green, yellow, and orange emissions due to Zn and Sn interstitials and oxygen vacancies in ZnO and SnO₂, respectively. It was observed that defects in ZnO overwhelmed defect states in SnO₂. The I - V measurements performed on thin heterofilms of ZnO/SnO₂ helped to determine the charge transfer route from ZnO to SnO₂ through defect states with an activation energy of 1.93 eV. The study confirmed that the defect states in type-II heterostructures can be used as charge storage for use at elevated temperatures in photocatalysis or energy harvesting devices

Acknowledgements

The work was funded by the Higher Education Commission of Pakistan through NRPU # 261, 1770 and PBAIRP-22-03. AF and AA are thankful to ICTP, Trieste, Italy for travel grants to conduct XPS in TASC Laboratories, Elettra, Trieste. Support provided by the Research Institute at KFUPM, Dhahran, is appreciated.

References

1. P. Agoston, A. Peter, M. Karsten, Risto, Nieminen, J.P. Martti, Intrinsic n-type behavior in transparent conducting oxides: a comparative hybrid-functional study of In₂O₃, SnO₂, and ZnO. *Phys. Rev. Lett.* 103, 245501 (2009)
2. Z. Fang, S. Weng, X. Ye, W. Feng, Z. Zheng, M. Lu, P. Liu, Defect engineering and phase junction architecture of widebandgap ZnS for conflicting visible light activity in photocatalytic H₂ evolution. *ACS Appl. Mater. Interfaces* 7, 13915 (2015)
3. H. Kaftelen, K. Ocakoglu, R. Thomann, S. Tu, S. Weber, E. Erdem, EPR and photoluminescence spectroscopy studies on the defect structure of ZnO nanocrystals. *Phys. Rev. B: Condens. Matter Phys.* 86, 014113 (2012)

4. A. Katoch, Z.U. Abideen, H.W. Kim, S.S. Kim, Grain-sizetuned highly H₂-selective chemiresistive sensors based on ZnO–SnO₂ composite nanofibers. *ACS Appl. Mater. Interfaces* 8, 2486 (2016)
5. H. Pan, V.A. Risley, K.R. Martindale, M.D. Heagy, Photocatalytic reduction of bicarbonate to formic acid using hierarchical ZnO nanostructures. *ACS Sustain. Chem. Eng.* 7, 1210 (2018)
6. D. Mohanta, K. Barman, S. Jasimuddin, M. Ahmaruzzaman, MnO doped SnO₂ nanocatalysts: activation of wide band gap semiconducting nanomaterials towards visible light induced photoelectrocatalytic water oxidation. *J. Colloid Interface Sci.* 505, 756 (2017)
7. S.W. Choi, A. Katoch, G.J. Sun, S.S. Kim, Synthesis and gas sensing performance of ZnO–SnO₂ nanofiber–nanowire stembranch heterostructure. *Sens. Actuators B* 181, 787 (2013)
8. Z. Wang, S. Gao, T. Fei, S. Liu, T. Zhang, Construction of ZnO/SnO₂ heterostructure on reduced graphene oxide for enhanced nitrogen dioxide sensitive performances at room temperature. *ACS Sens.* 4, 2048 (2019)
9. M. Lagariya, M. Modi, H. Dadhich, M. Gal, K. Gadani, P.S. Solanki, N.A. Shah, Studies on structural and electrical behaviors of chemically grown ZnO/SnO₂ nanocomposites. *Physica B* 577, 411774 (2020)
10. M. Madkour, Y.K. Abdel-Monem, F. Al, Sagheer, Controlled synthesis of NiO and Co₃O₄ nanoparticles from different coordinated precursors: impact of precursor's geometry on the nanoparticles characteristics. *Ind. Eng. Chem. Res.* 55, 12733 (2016)
11. Y.K. Abdel-Monem, S.M. Emam, H.M. Okda, Solid state thermal decomposition synthesis of CuO nanoparticles from coordinated pyrazolopyridine as novel precursors. *J. Mater. Sci.: Mater. Electron.* 28, 2923 (2017)
12. F. Azeez, E. Al-Hetlani, M. Arafa, Y. Abdel-Monem, A.A. Nazeer, M.O. Amin, M. Madkour, The effect of surface charge on photocatalytic degradation of methylene blue dye using chargeable titania nanoparticles. *Sci. Rep.* 8, 1 (2018)
13. A. Bumajdad, M. Madkour, Y. Abdel-Moneam, M. El-Kemary, Nanostructured mesoporous Au/TiO₂ for photocatalytic degradation of a textile dye: the effect of size similarity of the deposited Au with that of TiO₂ pores. *J. Mater. Sci.* 49, 1743 (2014)
14. Z. Zhang, M. Xu, L. Liu, X. Ruan, J. Yan, W. Zhao, T. Zhang, Novel SnO₂@ ZnO hierarchical nanostructures for highly sensitive and selective NO₂ gas sensing. *Sens. Actuators B* 257, 714 (2018)
15. S. Qin, P. Tang, Y. Feng, D. Li, Novel ultrathin mesoporous ZnO-SnO₂ nn heterojunction nanosheets with high sensitivity to ethanol. *Sens. Actuators B* 309, 127801 (2020)
16. A. Kar, S. Kundu, A. Patra, Surface defect-related luminescence properties of SnO₂ nanorods and nanoparticles. *J. Phys. Chem. C* 115, 118 (2011)
17. Y.Y. Liu, F. Liu, R. Wang, J.W. Luo, X. Jiang, R. Huang, L.W. Wang, Characterizing the charge trapping across crystalline and amorphous Si/SiO₂/HfO₂ stacks from first-principle calculations. *Phys. Rev. Appl.* 12, 064012 (2019)
18. J.F. Liao, W.Q. Wu, Y. Jiang, J.X. Zhong, L. Wang, D.B. Kuang, Understanding of carrier dynamics, heterojunction merits and device physics: towards designing efficient carrier transport layer-free perovskite solar cells. *Chem. Soc. Rev.* 49, 354 (2020)
19. K. Ghosh, R.K. Pandey, Fractal and multifractal analysis of n-doped ZnO thin films deposited on glass, ITO, and silicon substrates. *Appl. Phys. A* 125, 98 (2019)
20. V. Kumar, S.K. Singh, H. Sharma, S. Kumar, M.K. Banerjee, A. Vij, Investigation of structural and optical properties of ZnO thin films of different thickness grown by pulsed laser deposition method. *Physica B* 552, 221 (2019)
21. L. Liu, Z. Mei, A. Tang, A. Azarov, A. Kuznetsov, Q.K. Xu, X. Du, Oxygen vacancies: the origin of n-type conductivity in ZnO. *Phys. Rev. B* 93, 235305 (2016)
22. N. Ahmad, S. Khan, M.M.N. Ansari, Exploration of Raman spectroscopy, dielectric and magnetic properties of (Mn, Co) co-doped SnO₂ nanoparticles. *Physica B* 558, 131 (2019)
23. T. Bora, M.H. Al-Hinai, A.T. Al-Hinai, J. Dutta, Phase transformation of metastable ZnSnO₃ upon thermal decomposition by in-situ temperature-dependent Raman spectroscopy. *J. Am. Ceram. Soc.* 98, 4044 (2015)
24. S. Markovic, A. Stankovic, J. Dostanic, L. Veselinovic, L. Mancic, S.D. Skapin, D. Uskokovic, Simultaneous enhancement of natural sunlight- and artificial UV-driven photocatalytic activity of a mechanically activated ZnO/SnO₂ composite. *RSC Adv.* 7, 42725 (2017)
25. P.R. Talakonda, (2016), Excitation-intensity (EI) effect on photoluminescence of ZnO materials with various morphologies. *Luminescence: An Outlook on the Phenomena and their Applications* 91 (2016)

26. P.M. Kibasomba, S. Dhlamini, M. Maaza, C.P. Liu, M.M.Rashad, D.A. Rayan, B.W. Mwakikunga, Strain and grain size of TiO₂ nanoparticles from TEM, Raman spectroscopy and XRD: the revisiting of the Williamson–Hall plot method. *Results Phys.* 9, 628 (2018)
27. Z. Zhang, M. Choi, M. Baek, Z. Deng, K. Yong, Corrosion-assisted self-growth of Au-decorated ZnO corn silks and their photoelectrochemical enhancement. *ACS Appl. Mater. Interfaces* 9, 3967 (2017)
28. Y. Zou, S. Chen, J. Sun, J. Liu, Y. Che, X. Liu, D. Yang, Highly efficient gas sensor using a hollow SnO₂ microfiber for triethylamine detection. *ACS Sens.* 2, 897 (2017)
29. J. Kegel, V.Z. Zubialevich, M. Schmidt, I.M. Povey, M.E. Pemble, Effect of surface and defect chemistry on the photocatalytic properties of intentionally defect-rich ZnO nanorod arrays. *ACS Appl. Mater. Interfaces* 10, 17994 (2018)
30. C. Cheng, B. Liu, H. Yang, W. Zhou, L. Sun, R. Chen, H.J. Fan, Hierarchical assembly of ZnO nanostructures on SnO₂ backbone nanowires: low-temperature hydrothermal preparation and optical properties. *ACS Nano* 3, 3069 (2009)

Figure 3c shows the amplified image where the “d” spacing was 0.24 nm, which corresponded to (101) plane of ZnO and 0.34 nm, which corresponded to (110) plane of SnO₂. The TEM images clearly showed the dominance of ZnO as host material, where SnO₂ was embedded in it. The boundaries between the two regions were clearly identified and were marked by dashed lines. Figure 3d shows the SAED pattern of the same sample, i.e., grown at 1020 °C, which showed that the synthesized CNs had wurtzite phase of ZnO with (101) preferred direction and tetragonal rutile phase of SnO₂ with (110) preferred direction. SAED patterns were also used to determine the interplanar spacing,

